

Mechanism and Control of Combustion-Mode Transition in a Scramjet Engine

Toshinori Kouchi¹ and Goro Masuya²
Tohoku University, Sendai, Miyagi 980-8579, Japan

and

Tohru Mitani³ and Sadatake Tomioka⁴
Japan Aerospace Exploration Agency, Kakuda, Miyagi 981-1525, Japan

A sidewall compression scramjet engine operated in two combustion modes under Mach 6 flight condition, weak- and intensive-combustion modes. The weak mode occurred below the overall fuel equivalence ratio (Φ) of around 0.4. Transition from the weak mode to the intensive mode occurred at $\Phi \sim 0.4$, accompanied by a sudden increase in thrust. Mechanisms of the transition were numerically investigated in this study. Our simulations captured the sudden increase in thrust at the mode transition. In the weak mode, combustion occurred in only a region near the topwall where an igniter was installed. The combustion region expanded toward the cowl with boundary-layer separation at the mode transition. Our simulations demonstrated that low ignition capability resulted in the weak mode. We demonstrated that the presence of additional igniters on the sidewalls improved the ignition capability and achieved the intensive mode in the entire Φ range.

Nomenclature

$G_{H_2O_2}$	=	flame index ($= \nabla Y_{H_2} \cdot \nabla Y_{O_2}$)
H	=	engine height (= 250mm)
M	=	Mach number
P	=	pressure
T	=	temperature

¹ Assistant Professor, Department of Aerospace Engineering, Member AIAA

² Professor, Department of Aerospace Engineering, Senior Member AIAA

³ Fellow, Combined Propulsion Research Group, Member AIAA

⁴ Senior Researcher, Combined Propulsion Research Group, Senior Member AIAA

- Y_i = mass fraction of chemical species i
- W = engine width (= 200mm)
- x, y, z = stream-, height-, span-wise directions
- ΔF = thrust increment with combustion
- Δt = time step of simulation
- ϕ = local equivalence ratio
- Φ = overall equivalence ratio

Subscripts

- 0 = stagnation condition
- I = inlet condition
- W = value on wall

I. INTRODUCTION

SCRAMJET engine tests [1] indicated that the engine operated in two combustion modes for Mach (M) 4 and 6 flight conditions. Thrust measurements indicated that the engine hardly generated thrust when the overall fuel equivalence ratio (Φ) was below a threshold. Emission of the exhaust gas observed during the tests was weak. We refer to this lower thrust as the weak-combustion mode (weak mode). When the fuel equivalence ratio exceeded the threshold, combustion was active and the engine produced a large thrust. We refer to this much higher thrust as the intensive-combustion mode (intensive mode). Transition from the weak mode to the intensive mode occurred at $\Phi \sim 0.2$ for $M4$ flight condition, and that occurred in a range between $\Phi = 0.3$ and 0.6 for $M6$ flight condition. Both the flight condition and the engine configuration affected the threshold. The low thrust in the weak mode and the sudden increase in thrust with the transition are undesirable in a propulsion system. Therefore, it is necessary to analyze the mechanisms of the mode transition and to design an engine that attains the intensive mode in all Φ ranges.

Similar scramjet engines in the United States operate in the same combustion modes. Although Thomas et al. [2] reported a sudden increase in thrust under $M6$ flight condition, they did not mention its cause in open literature. Our group has experimentally investigated the transition mechanisms [3,4]. These mechanisms, however, have not yet been fully clarified. The experimental findings on each combustion mode are as follows.

- i) In the weak mode, the flame was detached from the fuel injectors and anchored on the topwall behind the shock wave from the cowl lip of the engine.
- ii) In the intensive mode, the flame was anchored at the backward-facing step upstream of the fuel injectors. The recirculation region at the step base merged with the separation bubble ahead of the fuel injector.
- iii) A reaction rate controlled combustion in the weak mode, whereas a fuel mixing rate controlled combustion in the intensive mode.

Based on these findings, previous works proposed two transition mechanisms. One was based on the formation of the merged-recirculation region when the fuel equivalence ratio (i.e., fuel injection pressure) increased [3]. The other focused on the upstream propagation of the combustion region in the weak mode [4].

The formation of the merged-recirculation region explained the transition mechanism as follow. High injection pressure produces high flow blockage due to the injection, enlarging the separation bubble ahead of the injector and combining the separation bubble with the recirculation region behind the step base. The merged-recirculation region provides a longer residence time for the fuel and ignition occurs in this region. As a result, the mode transition occurs. This mechanism does not consider the effects of downstream configuration in the combustor on the transition. Takahashi et al. [5] demonstrated that the mode transition occurred due to the changing geometry of the downstream section in the combustor at the same equivalence ratio. The intensive mode was attained in the constant-area combustor, and the weak mode was attained in the diverging combustors. Therefore, the formation of the merged-recirculation region does not completely explain the transition.

The other mechanism was based on the upstream propagation of the combustion region generated in the weak mode [4]. The mechanism was derived from comparison of the steady-state wall heating rates in the two combustion modes. We did not have reliable evidence for this mechanism because the mode transition is essentially an unsteady phenomenon.

Component tests of the scramjet combustor exhibited other mechanisms of the sudden increase in thrust. The component tests [6,7] indicated that the combustor operated in two modes: supersonic combustion and subsonic combustion with a precombustion shock wave in the isolator. The transition from supersonic combustion to subsonic combustion drastically increases the thrust. This might occur in an engine test. Dual-mode operation of the combustor is one of the transition mechanisms. The purpose of this study is to determine the transition mechanism (i.e., to verify which mechanism is appropriate).

Further information on mode transition is difficult to obtain from the experiments because of difficulties in measurement. Computational Fluid Dynamics (CFD) provides the details in both the flow-fields and the time evolution during the transition. Therefore, we used CFD in this study. Our previous simulations of the *M6* engine test did not simulate the mode transition, though the simulations effectively reproduced the data of the intensive mode [8,9]. The *M6* condition was at the limit of auto-ignition. A torch igniter was used in the engine test. Our previous simulations did not simulate the torch igniter: instead, the impulsive heating of the wall ignited the fuel. This seems to affect the mode transition. Therefore, we duplicated the torch igniter to simulate the mode transition in the present work.

II. DESCRIPTION OF NUMERICAL SIMULATION

A. Engine Configuration

Figure 1 presents the schematic diagram of the subscale scramjet engine simulated in this study. The x -axis is in the stream-wise direction, the y -axis is in the height-wise direction, and the z -axis is in the span-wise directions. The engine was rectangular with a length of $2.2m$; its entrance and exit were $200mm$ in width (W) and $250mm$ in height (H). The engine consisted of a cowl, a topwall, and two sidewalls. The engine was divided into four sections: an inlet, an isolator, a combustor, and a nozzle section. The combustor was divided into two sub-sections: a constant-area combustor and a diverging combustor. The inlet was a sidewall compression inlet swept back at 45 degrees. A strut was installed between the sidewalls. The geometrical contraction ratio of the inlet was 5.0 . The capture ratio was 0.81 . Rearward-facing steps with a height of $4mm$ were located on each sidewall at the entrance of the combustor. Twelve $1.5mm$ diameter fuel injectors were located downstream of the step on each sidewall. The orifices were spaced equally in the y -direction at an interval of $20mm$. Hydrogen fuel at room temperature was injected perpendicular to the flow at sonic speed. The fuel mass flow rate was $140g/s$, corresponding to $\Phi = 1$.

B. Grid System

The simulations in the engine were performed over a half-width of the flow-path, assuming symmetry about the center plane. An unstructured hybrid grid composed the three-dimensional computational domain [10]. The inlet section consisted of $7mm$ tetrahedrons. The tetrahedrons were 1.5 to $3mm$ in the constant-area combustor, $0.2mm$ in the fuel injector, and $5mm$ in the nozzle. The minimum distance from the wall was $10\mu m$. The computational grid

was optimized to capture the physically and chemically relevant features [11]. The domain consisted of 1.5 million control volumes.

C. Numerical Method

The computations were performed with the Tohoku University Aerodynamic Simulation (TAS) code, extended to reactive flow simulations by Kodera et al [12]. This code was applied to many internal and external flow simulations and was validated previously [8,9,12,13]. The code uses a cell-vertex, finite-volume technique with a second-order upwind scheme on a hybrid unstructured grid, to solve the three-dimensional compressible Reynolds-averaged Navier-Stokes equations with finite-rate chemistry. This platform employed the AUSM-DV scheme to approximate convective flux.

The LU-SGS implicit method [14] was used for time integration. Although this method saves the CPU cost because it requires no matrix inversion, it has less than first-order time accuracy. Generally, the Newton sub-iteration improves the time accuracy for unsteady flow simulations, but it was not used in this study. However, since the time step (Δt) was very small ($\Delta t = 10^{-8}s$) and fixed, the quantitative features of the time evolution of the flow-field were sufficiently captured.

The algorithm adopted the finite-rate hydrogen-oxygen reaction proposed by Stahl and Warnatz [15], which includes nine species (H_2 , O_2 , H_2O , H , HO_2 , OH , O , H_2O_2 , and N_2) and 17 elementary reactions. A one-equation turbulence model proposed by Goldberg and Ramakrishnan [16] was used to calculate turbulent eddy viscosity (ν_t). The turbulent Prandtl number was 0.9, and the turbulent Schmidt number (Sc_t) was 1.0. See Ref. 12 for details of this code.

D. Flow Condition

The simulation used the inflow conditions of the engine test [17]: $M_I = 5.3$, $P_I = 5.4kPa$ and $T_I = 250K$. These conditions corresponded to the $M6$ flight conditions with stagnation conditions of $P_0 = 4.8MPa$ and $T_0 = 1500K$, realized by a storage air heater of the engine test facility. The incoming flow dynamic pressure was $106kPa$. The Reynolds number based on H was 2.1×10^6 . The incoming boundary layer thickness was $50mm$, developed on the wall of the facility nozzle. The incoming boundary layer was modeled as a simple one-seventh power-law profile, and the boundary condition for the turbulence transport equation was same as the freestream value. Although the boundary conditions of the incoming boundary layer usually affect the shock-boundary layer interaction in the inlet

[18], they less affected in our computations because of boundary-layer bleeding on the topwall in the inlet. The thick incoming boundary layer easily induced flow separation due to combustion. It triggered an engine unstart. To prevent engine unstart and to extend the operating range of the engine, a boundary-layer bleed system was attached on the topwall. In the simulation, the bleeding velocity normal to the surface was assigned to fix the bleeding flow rate. Other flow properties on the bleed surface were extrapolated from the internal flow properties. The bleeding flow rate was 30g/s corresponding to 0.6% of the captured air in the inlet.

The *M6* flight condition was at the limit of the auto-ignition. Therefore, the engine was equipped with two torch igniters on the topwall at 20mm upstream of the step location (Fig. 1). Hydrogen/oxygen combustion gas with an equivalence ratio of 2.0 was injected at a chamber pressure of 650kPa through two 2.5-mm diameter orifices. The surplus H₂ mass flow rate of the igniter increased Φ less than 0.005. A one-dimensional equilibrium calculation [19] gave the boundary condition of the igniter. The calculated density, temperature, and velocity were imposed on the triangular cells of the topwall to simulate the igniter. The auxiliary igniters are depicted on the sidewall in Fig. 1. These igniters were not installed in the actual experiment. Details on the auxiliary igniters will be discussed later. Other solid walls were modeled as non-slip isothermal walls at a temperature of 300K.

III. RESULTS AND DISCUSSIONS

A. Comparison of CFD and Experimental Data

Our simulations with the igniter reproduced the engine test data of Ref. 17. Figure 2 presents the wall pressure (P_w) distributions on the sidewall along the engine with and without combustion. The horizontal axis is the distance from the leading edge of the topwall normalized by H . The vertical axis is P_w normalized by P_θ . The symbols denote the experiment data and the lines denote the numerical data. The computations properly reproduced the measured data in all cases.

The wall pressure distribution at $\Phi = 0.3$ (weak mode) was the same as that without fuel injection up to the region near the fuel injector. The pressure level at this mode was slightly higher in both the diverging combustor and the nozzle than that without fuel injection. The wall pressure at $\Phi = 0.5$ (intensive mode) increased steeply at the rear half of the isolator ($x/H \sim 3.3$) indicating the presence of precombustion shock in the isolator. The wall pressure increased remarkably around the fuel injectors at the combustor and at the nozzle, compared with those at $\Phi = 0.3$. In both cases, our simulations appropriately reproduce the experiment data.

Figure 3 illustrates the thrust increment with combustion (ΔF) as a function of Φ . The increment was evaluated by subtracting thrust without fuel injection from that with fuel injection and combustion. The dots denote the experiment data. The x and the line denote the numerical data. The computational trends of ΔF reproduced the measured data well, including the point of the mode transition.

The experiment data indicate that ΔF suddenly increased from $400N$ to $1500N$ at $\Phi = 0.3 \sim 0.4$, but drastically dropped to $100N$ at $\Phi \sim 0.7$. The mode transition occurred at $\Phi = 0.3 \sim 0.4$. The equivalence ratio at the transition was scattered in a certain Φ in the experiment. The rapid decrease in thrust at $\Phi \sim 0.7$ was caused by the combustor-inlet interaction. The intrusion of the precombustion shock wave into the inlet reduced both air capture and total pressure recovery. It increased the wall pressure in the inlet, increasing pressure drag. As a result, the thrust increment drastically decreased at $\Phi \sim 0.7$. We refer to this phenomenon as engine unstart. The numerical data indicated that the mode transition occurred at $\Phi \sim 0.4$ and that the engine unstart appeared over $\Phi \sim 0.55$. Our simulations did not accurately predict Φ at the engine unstart, but did predict Φ at the mode transition. The engine unstart depends on the development of flow separation on the topwall [8]. We believe the turbulence model greatly affects the growth rate of the separation: therefore, accurate prediction of this point is beyond our computations.

Figure 4a presents the computational local equivalence ratio (ϕ) at the exit of the engine, and Fig. 4b compares the computed and the measured data. The local equivalence ratio includes the fuel consumed by combustion. Figure 4a depicts a high ϕ region on the topwall but not on the sidewall. Thus, the uniformly injected fuel from the sidewalls accumulated on the topwall. The inlet had a swept-back angle to spill part of the incoming flow. The cowl interrupted this outward flow, and a strong shock wave emanated from the cowl lip. The pressure rise across the cowl shock wave induced the secondary flow toward the topwall in the sidewall boundary layers. As a result, two fuel vortices appeared on the topwall and produced a high ϕ region.

Figure 4b indicates that the simulation qualitatively reproduced those high fuel concentrations on the topwall. In this comparison, overall Φ was slightly different between the simulation and the experiment because the engine could not start above $\Phi = 0.6$ in the simulation. Therefore, the local ϕ was normalized by Φ . The simulation quantitatively overestimated ϕ/Φ at $y/H = 0.25$. This overestimation might be one of the reasons why the engine easily entered unstart in the simulations.

B. Flame Structures in Weak- and Intensive-Combustion Modes

Figure 5 depicts a three-dimensional view of OH radical distributions in the weak mode and in the intensive mode. The fuel was injected through 12 uniformly distributed orifices on each sidewall at $x/H = 4.34$. The igniter was installed on the topwall at $x/H = 4.19$ in the isolator. These figures demonstrate that the main part of the fuel at the cowl side did not burn in the weak mode, though it burned close to the fuel injectors in the intensive mode.

In the weak mode, OH radicals appeared only around the hot exhaust of the igniter on the topwall at x/H of 4.34. The surplus H_2 within the exhaust of the igniter reacted here. The main fuel from the injectors did not burn at this location. It was ignited near the topwall at x/H of 5.0. OH radicals appeared in the thick boundary layer on the topwall and the sidewall. The combustion region did not spread in the core flow in the weak mode.

In the intensive mode, small discrete flames appeared around the individual fuel jets at x/H of 4.34. The fuel jets near the topwall penetrated deeply into the airstream and reached the strut. The small discrete flame structures diminished at $x/H = 5$, because they consumed oxygen between the jets. As a result, a merged flame appeared in each flow-path: thus, the combustion region extended into the core flow downstream of the combustor.

We investigated the flame structures in each combustion mode by using the flame index parameter [20] defined as

$$G_{H_2O_2} = \nabla Y_{H_2} \cdot \nabla Y_{O_2} \quad (1)$$

This parameter distinguishes premixed flame from diffusion flame. In the regions where high temperature or high OH radical was detected, the index is positive for a premixed flame, to which oxidizer and fuel come from the same direction. In the regions where high temperature or high OH radical was detected, the index is negative for a diffusion flame, to which oxidizer and fuel come from opposite directions.

Figure 6 presents the cross-sectional flame index contours of the weak mode and the intensive mode. Combination of the flame index (Fig. 6) with OH radical (Fig. 5) distributions reveals premixed flames developed on the sidewall in the weak mode and diffusion flames developed in the core flow in the intensive mode.

In the weak mode, the small discrete negative index regions existed at $x/H = 4.34$. These negative regions indicate where H_2 /Air premixtures were generated, because ignition did not occur here. The positive regions appeared in front of the combustion zone on the sidewalls at $x/H \geq 6$, indicating that premixed flames developed in the weak mode. The secondary flow on the sidewall due to the cowl shock transported the mixtures to the topwall.

The premixtures were consumed in the premixed flames. As a result, OH radicals appeared in flames on the sidewall and topwall (Fig. 5a).

Generally, a premixed flame requires a stabilization mechanism because it is a self-sustaining propagation of the combustion zone. In the weak mode, the diffusion flame coexisted with the premixed flame near the topwall at $x/H = 5.0$. The diffusion flame worked as a flame holder for the premixed flame in the downstream section. The hot exhaust of the torch ignited the fuel injected from the orifice that was located near the topwall and formed the diffusion flame. Around that area, the flow speed was subsonic.

In the intensive mode, the negative index regions spread through the engine except at the $y/H \leq 1/4$ of $x/H = 4.34$ plane. At $x/H = 4.34$, small separated diffusion flames formed between the supersonic airstream and the fuel jets. These small discrete diffusion flames merged to form a large-scale diffusion flame at the downstream section. This large-scale diffusion flame formed around the rim of the longitudinal fuel vortex depicted in Fig. 4a. The positive index region at $x/H = 4.34$ appeared on the rim of the boundary-layer separation on the topwall. There, subsonic combustion occurred.

Mitani et al. [4] conducted the gas sampling measurement at the exit of the engine for each modes. The gas sampling data showed that a reaction rate controlled combustion in the weak mode, and a mixing rate of fuel controlled combustion in the intensive mode. The flame index and the OH radical distributions in our simulations indicates that a reaction rate controlled combustion in the weak mode, and a mixing rate controlled combustion in the intensive mode. Our simulations qualitatively reproduce the gas sampling measurement at the exit plane [4]. Thus, our simulation captured not only the mode transition point but also the flame structures at each combustion mode. Therefore, we conclude that our simulation is sufficiently accurate to investigate the mechanisms of the mode transition.

C. Transition Mechanisms

Combination of OH radical distribution and the flame index is useful for revealing flame structures even in a complicated flow-field such as in the engine. In this section, we analyze the mechanisms of the mode transition by using both the flame index and OH radical distributions of the transient CFD solutions from the weak to the intensive mode. Figures 7 present the time evolution of OH radical distribution on the sidewall. Figure 8 presents the flame index, and Fig. 9 presents the wall pressure distributions on the sidewall during the transition. Figures 7a, 8a, and 9a indicate the steady-state solutions in the weak mode at overall $\Phi = 0.37$ and, Figs. 7g, 8g, and 9g indicate

those in the intensive mode at $\Phi = 0.43$. The solutions were obtained after Φ impulsively increased from 0.37 to 0.43. Approximate time after the sudden increase in Φ is presented in each figure. The series of the transient CFD solutions demonstrated that the combustion region in the weak mode propagated to both the cowl side and the upstream side, due to combustion-generated high pressure. Upstream propagation was triggered for mode transition.

In the weak mode, the front of the reaction zone detached from the injector on the sidewall (Fig. 7a). The region where OH radicals were detected did not reach the cowl even at the exit of the engine. Most of the fuel near the cowl did not react. The positive index regions appeared in the combustion region (Fig. 8a). Thus, the flame in the weak mode was a premixed flame. The recirculation region behind the step base merged with the separation bubble ahead of each fuel injector. In addition, they connected with each other in the height-wise direction. Although a very large-recirculation region formed around the step, the intensive mode could not be attained. Our simulation clearly indicated that the formation of a merged recirculation region is insufficient to achieve the intensive mode.

At $1.85ms$ after Φ increased, a remarkable production of OH radicals appeared at the entrance of the diverging combustor of $y/H \sim 0.4$. Here the shock wave from the cowl crossed over the combustion region in the weak mode (Fig. 9b). Upstream propagation started from here. When the fuel mass flow rate increased, the diffusion flame around the torch, mentioned previously, expanded. It ignited the adjacent fuel jets convected by the secondary flow due to the cowl shock. OH radicals were remarkably produced within the boundary layer at this point. Local high pressure due to combustion pushed the hot products of combustion to both the cowl and upstream sides through the boundary layer (Figs. 7b and c). Local combustion within the boundary layer induced separation and shock wave. High temperature and pressure due to the shock wave sequentially induced auto-ignition at the core flow.

The front edge of the combustion region propagated at remarkable speed toward to the cowl side rather than the upstream side in the diverging combustor. It reached the cowl at $2.2ms$ and intruded into the constant-area combustor at $t \geq 2.2ms$. Propagation to the upstream side accelerated in the constant-area combustor. The speed relative to the wall in the diverging combustor was $400m/s$, and that in the constant-area combustor was $800m/s$.

The pressure rise with combustion was moderate in the diverging section because the geometrical expansion absorbed part of the thermal expansion due to combustion. However, all the thermal expansion was converted into the pressure rise in the constant-area section. As a result, the propagation speed in the constant-area combustor was higher than that in the diverging combustor. In the constant-area combustor, the wall pressure transiently exceeded $300kPa$ being over P_W in the steady intensive mode. Much high pressure in the constant-area combustor produced a

large separation bubble. The combustion region propagated upstream, associated with the separation bubble. The bubble size reached half of the flow-path height.

The front edge of the combustion region propagated along the shock wave from the cowl until it reached 2.4 ms. The combustion-generated high-pressure region spread like a wedge (Figs. 9b-e). The combustion-generated shock waves reflected on both the cowl and the topwall at 2.2ms. They promoted the upstream propagation of the combustion region on the cowl and the topwall. At 2.4ms, the combustion region at the mid-height reached into the backward-facing step, though it did not approach the topwall. Once ignition occurred in the recirculation region behind the step base, heated production due to combustion rapidly spread through the recirculation region, and ignition occurred there.

In the transient stage, the flame index was positive at the front of the combustion region (Fig. 8b-f). Flame propagated upstream in the transient stage, and the premixture of the weak mode was consumed. Once the flame was anchored at the step base, negative index regions appeared in front of the positive index region (Fig. 8g). A diffusion flame developed after the premixture was consumed. In the steady-state solution, the flame index became negative around the step base. In the intensive mode, supersonic combustion occurred in the shear layers between the supersonic airflow and the fuel jets. The separation bubble generated in the transient stage disappeared except on the topwall. In summary, we conclude that the weak mode originated from the low ignition capability.

D. Achievement of the Intensive Mode by Auxiliary Igniters

Improvement of both ignition and flame holding at the cowl side is key to controlling the mode transition, because the weak mode originated from the low ignition capability. Therefore, we improved ignition capability by adding auxiliary igniters on the sidewall, and numerically demonstrated that they prevented the weak mode and attained the intensive mode in the entire Φ range. Figure 1 indicates the locations of the auxiliary igniters. One auxiliary igniter was installed near the cowl, and another at the center of the sidewall. They operated under the same conditions as the igniter installed on the topwall. Their orifice diameters were 2.5mm.

Figures 10 and 11 present the OH radical and the flame index distributions on the sidewall during the transitional stages after starting the auxiliary igniters. Fuel equivalence ratio was kept at overall $\Phi = 0.15$, and the engine operated in the weak mode unless the auxiliary igniters were operated. Figures 10a and 11a indicate the solutions before the auxiliary igniters were operated.

At $0.1ms$ after the auxiliary igniters were operated, OH radicals appeared around the auxiliary igniters (Fig. 10b). They spread downstream and merged together at $0.2ms$. At $0.3ms$, the combustion regions due to the auxiliary igniters merged with the combustion region in the weak mode inducing high pressure in the constant-area combustor and on the topwall. The high pressures pushed the combustion region toward the step (Figs. 10d, e and f). Simultaneously, the combustion region spread downstream and covered the sidewall as time passed. The high OH radical region at the transitional stage gradually disappeared, and the intensive mode was achieved (Fig. 10g).

The auxiliary igniters produced positive index regions around them (Fig. 11b), and ignited the premixture near the fuel injectors. These positive index regions expanded toward the downstream section and pushed away the negative index regions to the step, except near the cowl (Figs. 11c-f). The premixed flames propagated while consuming the premixture. The index around the step changed from positive to negative (Figs. 11f and g) indicating that the diffusion flame was established and the intensive mode was attained after the flame reached the step base and was held there.

In the steady-state solution with the auxiliary igniters, the diffusion flame system, like that at $\Phi > 0.43$ without the auxiliary igniters, appeared in the combustor, except near the cowl. Near the cowl, the premixed flame coexisted with the diffusion flame. The cowl-side auxiliary igniter stabilized the premixed flame: it operated not only as an igniter but also as a flame holder. The forced ignition with the auxiliary igniters produced a high combustion efficiency of 0.97 and a high ΔF of $530N$. Thus, the auxiliary igniter improved, ignition capability at the far-low Φ of 0.15. The auxiliary igniter near the cowl is effective for achieving the intensive mode in the entire Φ range.

IV. CONCLUSION

Numerical simulations in the scramjet engine, which had backward-facing steps on the sidewalls in front of the fuel injectors for flame-holding, were used to investigate the mechanisms of the combustion mode transition. The simulations were conducted under Mach 6 flight conditions, with the stagnation conditions of 4.8MPa and 1500K. Our simulations captured the sudden increase in thrust with the mode transition by simulating the ignition process with the igniter installed on the topwall.

During the weak-combustion mode, the main fuel from the sidewall did not ignite near the fuel injectors. The combustion region was confined within the boundary layer both on the topwall and the sidewall near the topwall

side. However, in the intensive-combustion mode, a diffusion flame was established between the supersonic airflow and the fuel jets. It was anchored with a backward-facing step.

The mode transition was induced by upstream propagation of the combustion region with boundary-layer separation in the weak-combustion mode. It started where the shock wave from the cowl lip crossed over the combustion region in the weak-combustion mode. The driving force of the transition was combustion-generated high pressure.

In the present engine, the ignition capability was too low to obtain the high pressure for inducing the intensive-combustion mode at the low equivalence ratio regime. Numerical demonstration indicated that the installation of auxiliary igniters on the sidewalls improved ignition capability and delivered higher thrust at a low equivalence ratio. The auxiliary igniters prevented the sudden change in thrust that was unfavorable for engine control.

Acknowledgments

The computations were carried out on the Kakuda Space Center's NEC SX-6 of JAXA in Japan. The authors acknowledge for the generous allocation of the SX-6 time.

References

- [1] Chinzei, T., Mitani, T., and Yatsuyanagi, Y., "Scramjet Engine Research at the National Aerospace Laboratory in Japan," *Scramjet Propulsion*, edited by E.T. Curran and S.N.B. Murthy, Progress in Astronautics and Aeronautics Vol. 189, AIAA, New York, 2001, pp. 159-222.
- [2] Thomas, S.R., and Guy, R.W., "Scramjet Testing From Mach 4 to 20 Present Capability and Needs for the Nineties," AIAA paper 1990-1388, 1990.
- [3] Kanda, T., Kudo, K., and Murakami, A., "Combustion with Boundary Layer / Fuel Jet Interaction in a Scramjet Combustor," *Proceedings of Fluids Engineer Conference 2000*, pp. 209-214, 2000 (in Japanese).
- [4] Mitani, T., Chinzei, N., and Kanda, T., "Reaction and Mixing-Controlled Combustion in Scramjet Engines," *Journal of Propulsion and Power*, Vol. 17, No. 2, pp. 308-314, 2001. [DOI: 10.2514/2.5743]
- [5] Takahashi, S., Yamano, G., Wakai, K., Tsue, M., and Kono, M., "Flowfield in a Model Scramjet Combustion in Case of Injecting Fuel Perpendicularly behind the Backward-Step," *Journal of the Japan Society for Aeronautical and Space Science*, Vol. 47, No. 548, pp. 333-339, 1999 (in Japanese).
- [6] Sullins, G.A., "Demonstration of Dual Mode Transition in a Scramjet Combustor," *Journal of Propulsion and Power*, Vol. 9, No. 4, 1993, pp. 515-520. [DOI: 10.2514/3.23653]

- [7] Le, D.B., Goynes, C.P., Krauss, R.H., and McDaniel, J.C. "Experimental Study of a Dual-Mode Scramjet Isolator," *Journal of Propulsion and Power*, Vol. 24, No. 5, 2008, pp. 1050-1057. [DOI: 10.2514/1.32591]
- [8] Kouchi, T., Mitani, T., and Masuya, G., "Numerical Simulations in Scramjet Combustion with Boundary-Layer Bleeding," *Journal of Propulsion and Power*, Vol. 21, No. 4, pp. 642-649, 2005. [DOI: 10.2514/1.7967]
- [9] Mitani, T., and Kouchi, T., "Flame Structures and Combustion Efficiency Computed for A Mach 6 Scramjet Engine," *Combustion and Flame*, Vol. 142, pp. 187-196, 2005. [DOI: 10.1016/j.combustflame.2004.10.004]
- [10] Ito, Y., and Nakahashi, K., "Unstructured Mesh Generation for Viscous Flow Computations," *Proceedings of the 11th International Meshing Roundtable*, pp. 367-377, 2002.
- [11] Kouchi, T., Mitani, T., and Masuya, G., "Problems of Numerical Diffusion Found in Scramjet," AIAA paper 2005-3216, 2005.
- [12] Kodera, M., Sunami, T., and Nakahashi, K., "Numerical Analysis of Scramjet Combusting Flows by Unstructured Hybrid Grid Method," AIAA paper 2000-0886, 2000
- [13] Nakahashi, K., Ito, Y., and Togashi, F., "Some challenges of realistic flow simulations by unstructured grid CFD," *International Journal for Numerical Methods in Fluids*, Vol. 43, pp. 769-783, 2003. [DOI: 10.1002/flid.559]
- [14] Sharov, D., and Nakahashi, K., "Reordering of Hybrid Unstructured Grids for Lower-Upper Symmetric Gauss-Seidel Computations," *AIAA Journal*, Vol. 36, No. 3, pp. 484-486, 1998. [DOI: 10.2514/2.392]
- [15] Stahl, G., and Warnatz, J., "Numerical investigation of time-dependent properties and extinction of strained methane- and propane-air flamelets," *Combustion and Flame*, Volume 85, Issue 3-4, pp. 285-299, 1991.
- [16] Goldberg, U. C., and Ramakrishnan, S. V., "A Pointwise Version of Baldwin-Barth Turbulence Model," *Computational Fluid Dynamics*, No. 1, pp. 321-338, 1993. [DOI: 10.1080/10618569308904478]
- [17] Ueda, S., Tomioka, S., Ono, F., Sakuranaka, N., Tani, K., and Murakami, A., "Mach 6 Test of a Scramjet Engine with Multi-Staged Fuel Injection," AIAA paper 2006-1027, 2006.
- [18] Kodera, M., Nakahashi, K., and Sharov, D., "Simulation of 3D shock Wave/Turbulent Boundary Layer Interactions by Hybrid Grid Method," *Transactions of the Japan Society of Mechanical Engineers, Series B*, Vol. 64, No. 627, 1998. [in Japanese].
- [19] Gordon, S., and McBride, B.J., "Computer Program for the Calculation of Complex Equilibrium Composition," NASA SP-273, 1971.
- [20] Yamashita, H., Shimada, M., and Takeno, T., "A Numerical Study on Flame Stability at The Transition Point of Jet Diffusion Flames," *Proceedings of 26th Symposium (International) on Combustion*, 27-34, 1996.

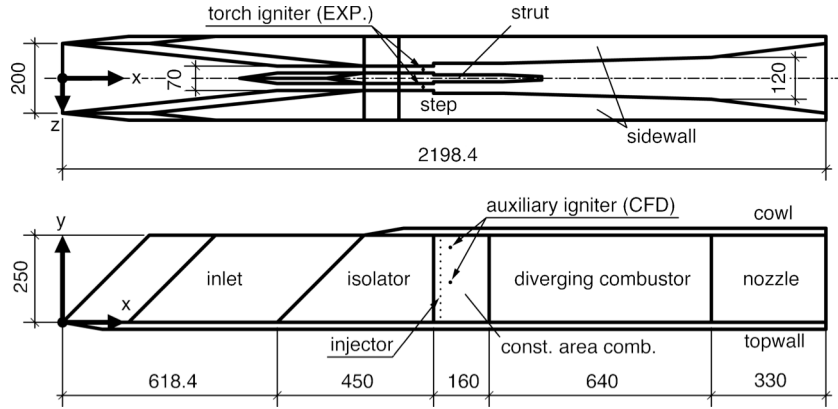


Fig. 1 Schematic diagram of sidewall compression type scramjet engine

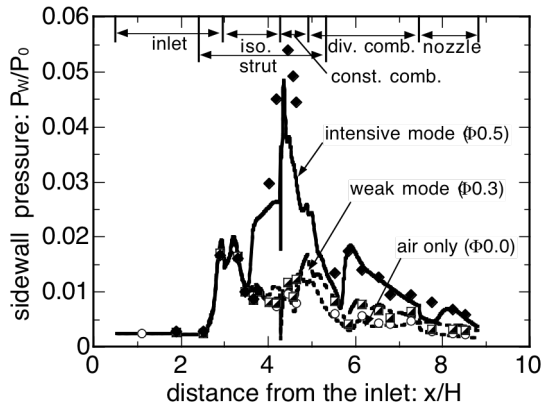


Fig. 2 Comparison of wall pressure measured on the experiments and those by the simulations.

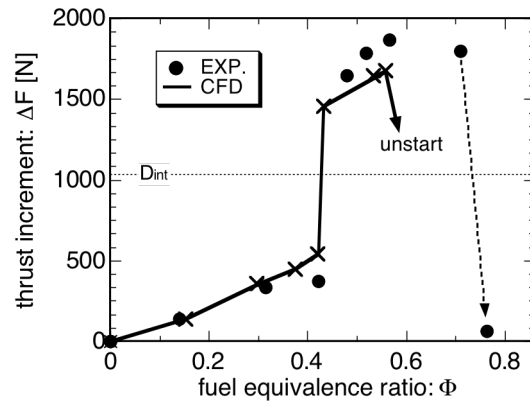


Fig. 3 Thrust increment as function of fuel equivalence ratio; comparison of measured data and numerical ones.

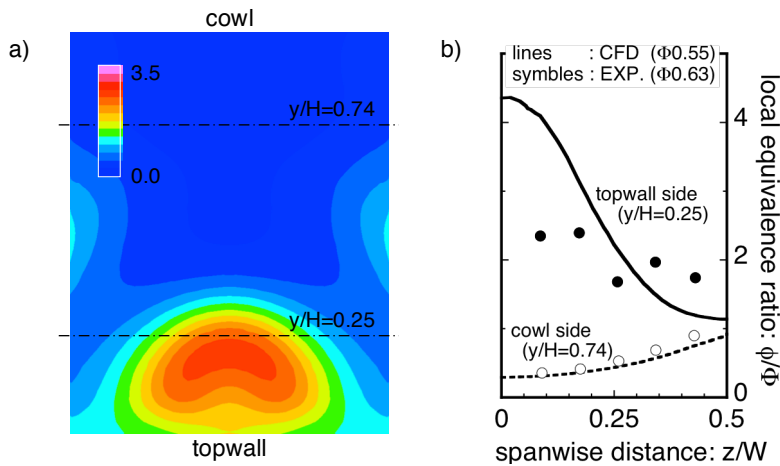


Fig. 4 Local equivalence ratio at the exit of the engine; a) numerical result at $\Phi = 0.55$ b) comparison of experimental data and numerical one.

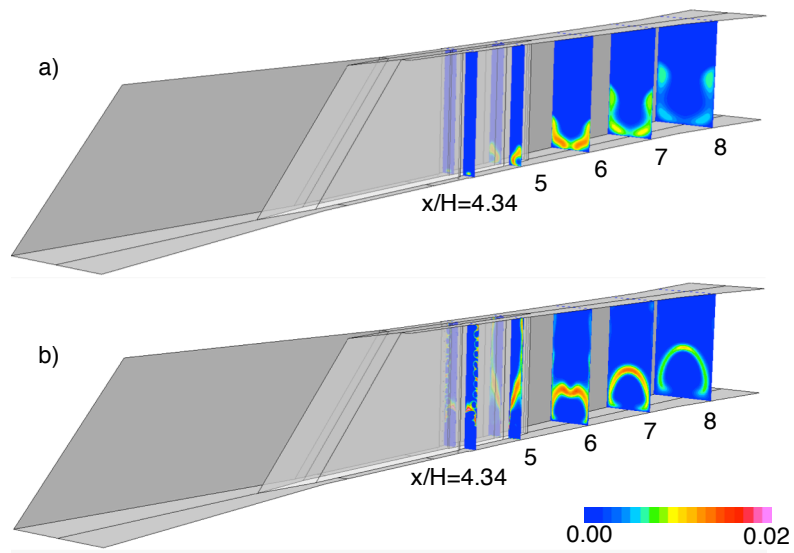


Fig. 5 Cross-sectional OH radical distributions at a) weak-combustion mode at $\Phi = 0.3$ and b) intensive-combustion mode at $\Phi = 0.53$.

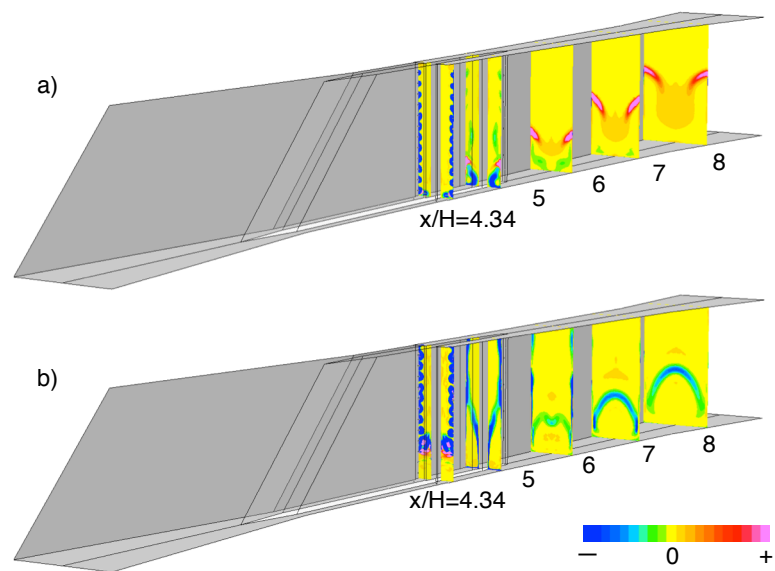


Fig. 6 Cross-sectional flame index $(\nabla Y_{H_2} \cdot \nabla Y_{O_2})$ distributions at a) weak-combustion mode at $\Phi = 0.3$ and b) intensive-combustion mode at $\Phi = 0.53$.

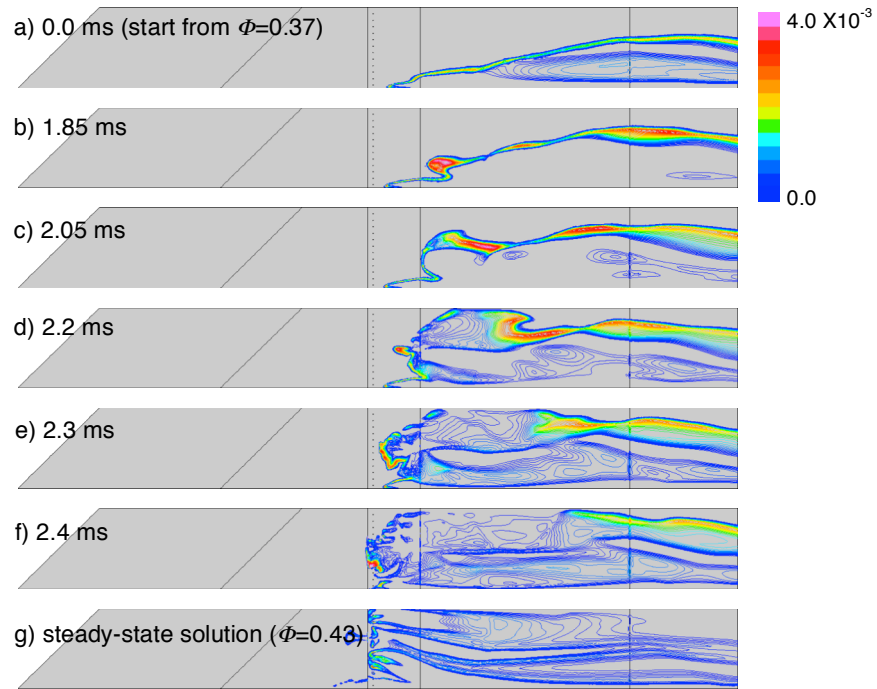


Fig. 7 Time evolution of OH radical distributions on the sidewall from weak- to intensive-combustion mode.

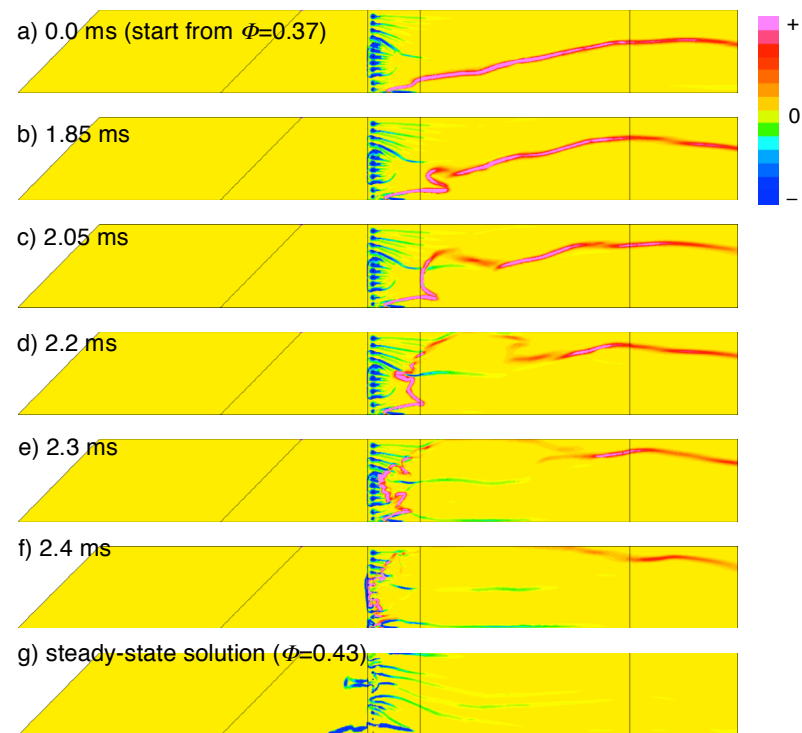


Fig. 8 Time evolution of flame index distributions on the sidewall

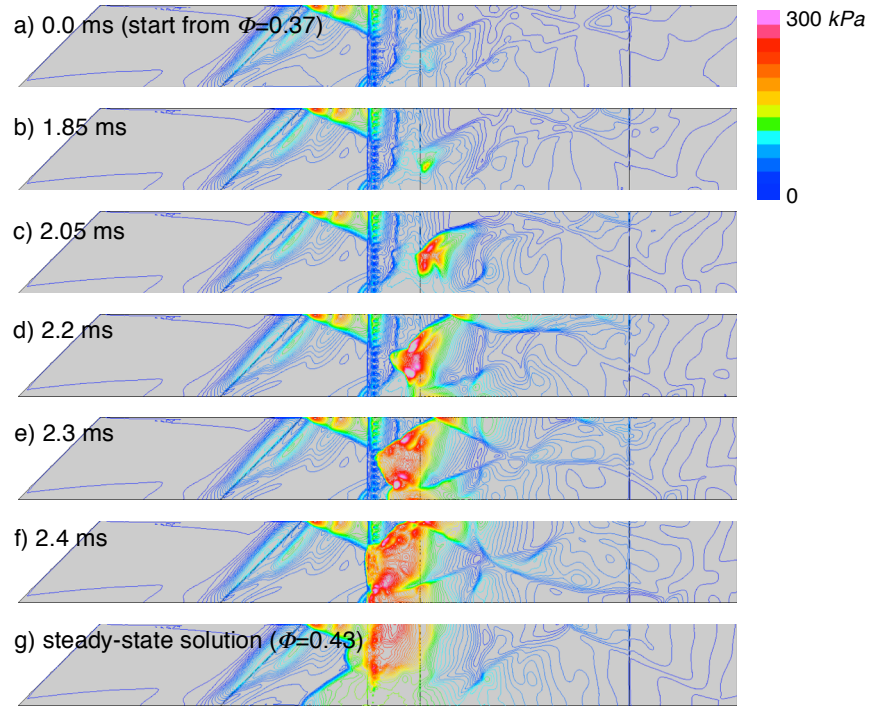


Fig. 9 Time evolution of wall pressure distributions on the sidewall from weak- to intensive-combustion mode.

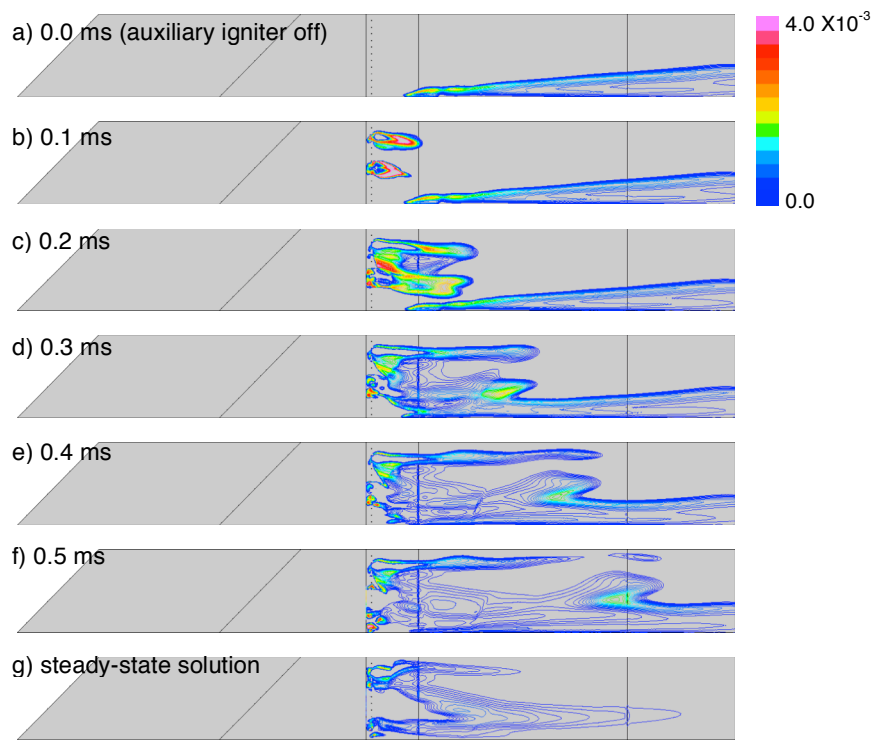


Fig. 10 Change in OH radical distributions on the sidewall after auxiliary igniters operated: $\Phi = 0.15$.

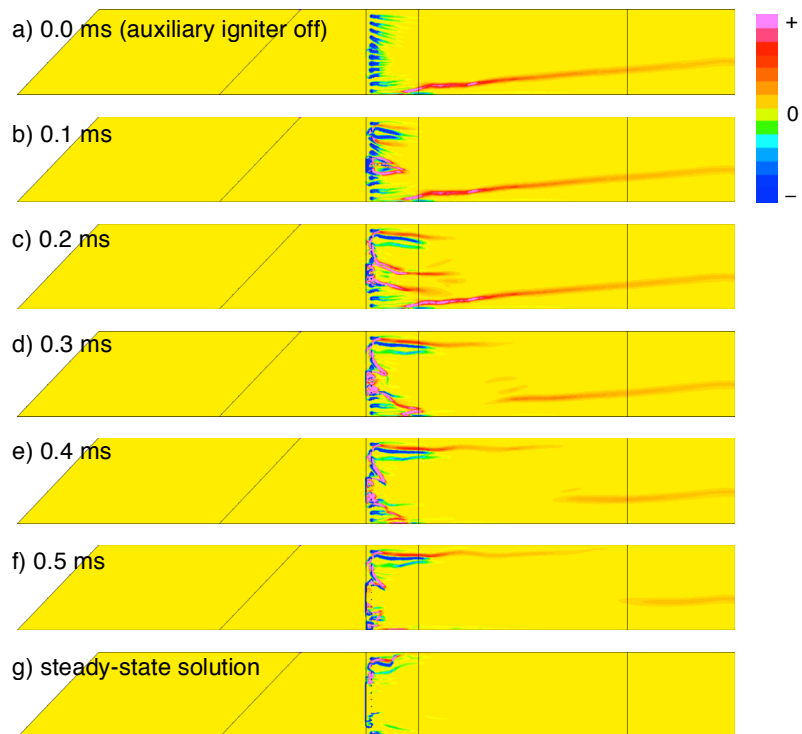


Fig. 11 Change in flame index distributions on the sidewall after auxiliary igniters operated: $\Phi = 0.15$.